


Self-Oscillations in a Nanogap Spin Hall Nano-Oscillator with a Perpendicularly Magnetized External Film

Lina Chen,^{1,2} Kaiyuan Zhou,² Zui Tao,² Zhenyu Gao,² Like Liang^{①,2}, Zishuang Li,² and Ronghua Liu^{②,*}

¹*School of Science, Nanjing University of Posts and Telecommunications, Nanjing 210023, China*

²*Jiangsu Provincial Key Laboratory for Nanotechnology, National Laboratory of Solid State Microstructures and School of Physics, Nanjing University, Nanjing 210093, China*

 (Received 15 August 2022; revised 8 January 2023; accepted 13 April 2023; published 15 May 2023)

We study spin-current-induced magnetodynamics in a planar nanogap spin Hall nano-oscillator (SHNO) based on Pt/[Co/Ni]₄ with a large perpendicular magnetic anisotropy (PMA) in in-plane field geometry. Two distinct dynamic modes are observed in the spin-torque ferromagnetic resonance (FMR) and the generated microwave spectra. The primary mode has a frequency above the FMR frequency and a significant blueshift of the frequency with the increasing current I , consistent with the propagating spin-wave mode. The secondary higher-frequency mode with a much weaker power intensity, discrete frequency jump, and a slight redshift of frequency is only observed at low fields below the saturation field of 2 kOe, suggesting that it is likely related to the emerged domain region with in-plane magnetization due to grain-boundary defects, which is further supported by the frequency enhancement with reducing temperature. The primary propagating mode decreases its frequency and broadens its minimum linewidth by reducing the temperature, indicating that the frequency-drift instability dominates its dynamical decoherence due to the boundary-pinning effect. Furthermore, the micromagnetic simulation reproduces the experimentally observed propagating spin-wave and in-plane domain modes, and provides their spatial characteristics. Our demonstrated propagating spin waves in a SHNO with an out-of-plane magnetization extended bilayer can facilitate long-distance mutual synchronization in the SHNO network arrays for enhancing coherence and power as spin-wave sources in magnon-based devices or spin-based neuromorphic computing.

DOI: [10.1103/PhysRevApplied.19.054051](https://doi.org/10.1103/PhysRevApplied.19.054051)

I. INTRODUCTION

The recently demonstrated spin-orbit torque (SOT), in magnetic heterostructures with heavy nonmagnetic metals or topological materials, provides an attractive alternative to spin-transfer torque (STT) in magnetization auto-oscillations [1,2] and switches [3–6], such as magnetic random-access memory (MRAM). Different from STT [7,8], SOT exerted from pure spin currents does not require the charge current to flow through the actual magnetic layer of devices, consequently minimizing current-induced local Joule heating and Oersted field side effects [9–11], and further expanding the spintronic materials into the ultralow damping magnetic insulators to facilitate the development of energy-efficient spin-wave-based devices [12–14]. Among such devices, spin Hall nano-oscillator (SHNO), a device that can generate controllable spin wave on the nanoscale, has significantly benefited from such flexibility, e.g., adopting various device structures and different magnetic materials [1,2,13–21]. Moreover, thanks to the intrinsic nonlinearity, SHNOs can synchronize well

with the external rf source [22–24] and other SHNOs in one-dimensional chains [25] and two-dimensional arrays [26]. Such mutual synchronization behavior can be used to achieve high-speed and low-power neuromorphic computing in SHNO network arrays [26,27]. However, the prior SHNOs, including triangular nanogap and vertical nanocontact on the extended magnetic films [28,29], nanoconstrictions [30,31], and nanowires [32], exhibit a localized nature with a significantly negative nonlinearity due to the easy-plane magnetic anisotropy [28,33], the geometry-induced substantial local dipolar field [18,30], and current-induced local Oersted field opposite to the external magnetic field [29]. The localized spin waves with the frequency below the spectrum of linear spin-wave modes (e.g., self-localized bullet [1,2,33] and dynamical bubble or skyrmion modes [15,34,35]) are disadvantages to the mutual synchronization over long distances and further impede the implementation of the efficient nonlinear interaction SHNO network arrays for the wave-based computing [26,27].

Fortunately, the nonlinear auto-oscillator theory, proposed by Slavin and Tiberkevich [36], indicates that the magnetodynamics nonlinearity is highly related to

*rhliu@nju.edu.cn

the magnetic anisotropy of thin film. The local spin-wave mode with a negative nonlinearity coefficient \aleph in magnetic thin film with the easy-plane shape anisotropy can be tuned to the propagating mode by bringing in strong perpendicular magnetic anisotropy (PMA) or out-of-plane oblique magnetic field to counteract the shape anisotropy. A few previous reports also prove that SOT-driven propagating spin waves can be achieved in SHNOs based on the extended Bi-substituted yttrium iron garnet (BiYIG) films with large PMA under in-plane magnetic field [37] and nanoconstriction W/Co-Fe-B/MgO or Ta/Pt/[Co/Ni]_n/Co/AlO_x stacks with substantial PMA and its frequency can be tuned by the electric field [38–41]. Since the static magnetization configuration of the magnetic thin film with PMA highly depends on the in-plane field below its saturation field, we expect the nanogap SHNO consisting of such PMA magnetic multilayer to exhibit different magnetodynamics behaviors.

Here, we study the current-driven magnetodynamics of the planar nanogap SHNO based on Pt/[Co/Ni]₄ with a large PMA ($H_k = 8.3$ kOe) at an in-plane field geometry by spin-torque ferromagnetic resonance (STFMR) and microwave spectroscopy. Below the saturation magnetic field $H_s \sim 2$ kOe, we observe two types of dynamical modes with distinct frequencies, intensities, and frequency dependences on the excitation current. The primary lower-frequency mode has a significant power intensity, and its frequency near the FMR frequency f_{FMR} at small currents and above f_{FMR} at large currents, and exhibits a significant frequency blueshift with increasing current I . It is identified as a propagating spin-wave mode corresponding to the perpendicular magnetization region. In contrast, the secondary higher-frequency mode is considered to be the mode related to the in-plane magnetization (IM) domain region with a small PMA at grain-boundary defects near the active device region because it shows a much weaker power intensity and slight frequency redshift with current, as well as a discrete frequency jump with varying magnetic field. The temperature dependence of spectra characterized by the frequency decrease (increase) with reducing the temperature for the former (the latter) due to the enhancement of PMA further confirms the above argument. In contrast to the previously reported thermal broadening for the self-localized bullet mode in the in-plane magnetization Pt/Py-based SHNOs, the minimum linewidth of the primary propagating mode becomes wider with reducing the temperature. Hence we infer that SOT-driven dynamical coherence in the studied Pt/[Co/Ni]-based SHNO with a strong PMA is dominated by the pinning effect due to the spatial magnetization inhomogeneity or domain structures. Our demonstrated low-field controllable propagating spin wave in the extended magnetic film-based SHNOs can be utilized to develop SHNO network arrays with neuromorphic functionalities.

II. EXPERIMENTAL RESULTS AND DISCUSSION

A. Magnetization characteristics of the film

The device is based on Pt(4)/[Co(0.2)/Ni(0.3)]₄ (Pt/[Co/Ni]) multilayers with a strong PMA, deposited on sapphire substrates at room temperature by magnetron sputtering with Ar pressure approximately 3×10^{-3} Torr. All thicknesses are given in nanometers. The magnetic properties of the multilayer are characterized by the field-dependent magnetic susceptibility and magneto-optic Kerr effect (MOKE) microscopy of the film and the anomalous Hall resistance (AHR) of a microscale Hall cross. Figure 1(a) shows the magnetization hysteresis curves with the out-of-plane H_{\perp} and in-plane field H_{\parallel} geometries for the film sample. A square $M - H$ loop under out-of-plane fields (red circles) indicates that the magnetic film exhibits a well-defined PMA. The obtained saturation magnetization M_s of approximately 600 emu/cm^3 is consistent with the previous reports [42]. Based on the out-of-plane and in-plane magnetization hysteresis loops, the perpendicular anisotropy field $H_k \sim 8.2$ kOe can be determined by using the following formula for magnetic thin film systems: $H_k - 4\pi M_s = (2/M_s)(\int_0^{M_s} H_{\perp} dM - \int_0^{M_s} H_{\parallel} dM)$. The magnetic properties of the magnetic film also can be revealed by magnetotransport, e.g., anomalous Hall effect (AHE). Figure 1(b) shows the out-of-plane and in-plane AHR loops as a function of the applied magnetic fields for a microscale Hall cross. Similar to the $M - H$ loop, a sharp square hysteresis loop obtained with the field perpendicular to the film plane indicates a good PMA. The hysteresis loop measured with the field oriented at $\varphi = 5^\circ$ relative to the film plane is more rounded and broader, and the maximum Hall resistance achieved at small H is noticeably smaller. These behaviors are consistent with the magnetization reversal by the gradual nucleation and the growth of magnetic bubble domains, as demonstrated by MOKE imaging [Fig. 1(c)]. The H_k of 8.0 kOe calculated from the in-plane AHR loop is close to the value of 8.2 kOe determined by the $M - H$ loops above.

B. STFMR spectra of micro- and nanoscale devices

To investigate the magnetization dynamics of the magnetic film with a strong PMA and magnetic bubble or stripe domains under moderate in-plane magnetic fields, we adopt the STFMR technique to characterize the FMR spectra of the microscaled Pt/[Co/Ni] thin film and the in-plane nanogap SHNO. The STFMR and magnetization auto-oscillation can be excited by applying a rf current I_{rf} or a dc current I_{dc} between the electrodes resulting in a spin current locally injected into the adjacent FM layer due to the combination of the spin Hall effect in Pt [9–11] and the Rashba effect at the interface [43,44]. All the spectra measurements of the device described below are performed with H tilted by $\varphi = 5^\circ$ and $\theta = 60^\circ$, which

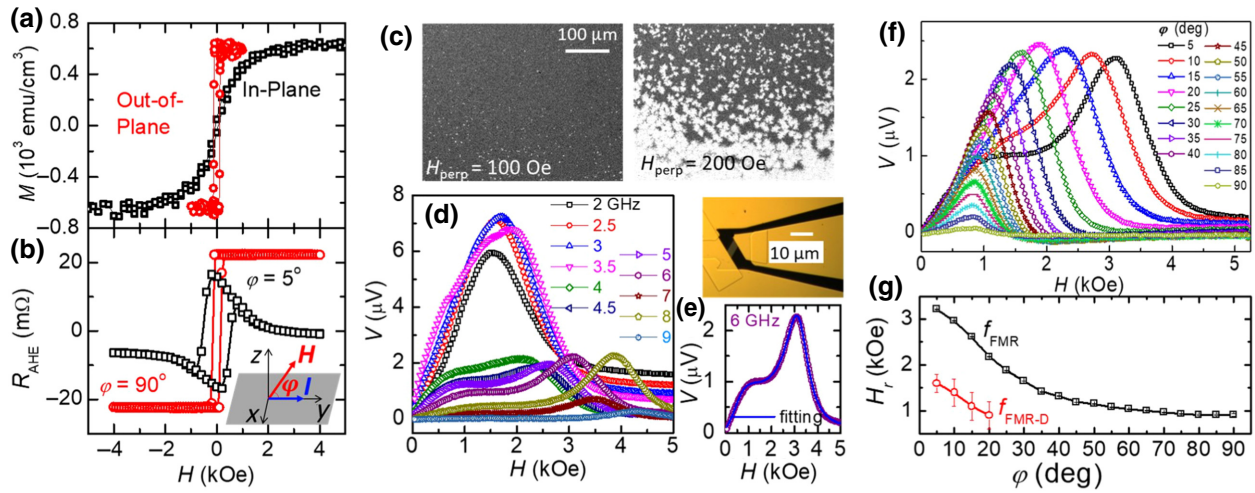


FIG. 1. Magnetic characteristics of the Pt(4)/[Co(0.2)/Ni(0.3)]₄ film at 295 K. (a) Magnetization loops of the film with out-of-plane (red circles) and in-plane (black squares) magnetic field. (b) Anomalous Hall effect measured in a film patterned into a $4 \times 14 \mu\text{m}$ Hall bar, with out-of-plane (red circles) and near in-plane (black squares) field. The out-of-plane field tilting angle φ is defined in the inset of (b). (c) The magnetic domain images of the film obtained by MOKE microscopy at two representative out-of-plane magnetic fields $H_{\text{perp}} = 100$ and 200 Oe. (d) STFMR spectra with the excitation frequency f range of 2–9 GHz at field forming an in-plane angle $\theta = 60^\circ$ with respect to the current direction and an out-of-plane tilting angle $\varphi = 5^\circ$ from the film plane. (e) Representative STFMR spectrum showing two FMR peaks obtained at $f = 6$ GHz (symbols) and its fitting curve with two Lorentzian functions (solid line). Top panel of (e): the optical microscope image of the device for the STFMR experiment of the $5 \times 10 \mu\text{m}$ rectangular shape. (f) STFMR spectra with the out-of-plane tilting angle φ from 5° to 90° with a step of 5° at the excitation frequency $f = 6$ GHz and $\theta = 60^\circ$. (g) The resonance fields H_r of f_{FMR} and $f_{\text{FMR-D}}$ modes, defined in the main text, as a function of φ .

enables the generation of the sizeable mixing dc voltage for STFMR measurement and microwave voltages for spin-torque auto-oscillation due to the combination of the anisotropy magnetoresistance (AMR) and spin Hall effect-generated spin-orbit-torque effects.

Figure 1(d) shows the STFMR spectra of a microscale stripe, as illustrated in the top panel of Fig. 1(e), which are recorded by scanning the applied magnetic field under the different excitation frequencies f from 2 to 9 GHz and $\theta = 60^\circ$ and $\varphi = 5^\circ$. The STFMR spectral has a primary peak at the high fields and a weak broader peak at the low fields. The two resonance fields H_r are determined by fitting the FMR spectrum with two Lorentzian functions [see Fig. 1(e)]. From the f versus H_r dispersion relations and power intensity of the FMR spectra, we determine that the primary high-field peak corresponds to the FMR mode of the primary PMA regime f_{FMR} , and the weak low-field peak is ascribed to the FMR mode of the bubble and stripe domain wall or IM domain region due to grain-boundary defects or inhomogeneous PMA, labeled as $f_{\text{FMR-D}}$. The significant peak broadening for these two FMR modes in the micro-sized thin film is also consistent with the spatial inhomogeneity of magnetization and stray field due to existence of multiple magnetic bubble or IM domains under the applied in-plane field. To further confirm this, we perform STFMR measurements with the out-of-plane tilting angle φ from near in-plane (5°) to out-of-plane (90°) with a step of 5° at the fixed $f = 6$ GHz and $\theta = 60^\circ$, as

shown in Fig. 1(f). Figure 1(g) shows the extracted resonance fields H_r of f_{FMR} and $f_{\text{FMR-D}}$ as a function of φ . The weak broader peak $f_{\text{FMR-D}}$ appears only for the low tilting angles $\varphi \leq 20^\circ$, consistent with the fact that the out-of-plane magnetic field can merge the magnetic domain structures.

We also measure the STFMR spectra of the active SHNO to explore further the dynamical characteristics of the Pt/[Co/Ni] layer in the nanoscale active region of the SHNO. The nanogap SHNO consists of the Pt/[Co/Ni] multilayer disk with a $2\text{-}\mu\text{m}$ -diameter and two-pointed Au(100) electrodes, which are separated by an approximately 100-nm gap, and are fabricated on top of the disk [Fig. 2(a)]. Figure 2(b) shows the STFMR spectra of the nanogap SHNO with different excitation frequencies f from 2 to 6 GHz with a step of 0.5 GHz. Similar to the micro-sized strip device above, the nanogap SHNO also exhibits two individual peaks in the FMR spectra for the low excitation frequencies. However, the two spectral peaks are more narrow than that of the micro-sized stripe device, which further confirms the above argument that the low-field peak is related to the FMR mode of the nanoscale IM domain or bubble and stripe domain wall $f_{\text{FMR-D}}$, which is significantly broadened or mixed by appearing multiple bubble and stripe domain structures in the micro-size samples [Fig. 1(c)]. The microscale stripe and the nanogap SHNO have the same f versus H_{res} dispersion relations for both the primary FMR f_{FMR} and the secondary

domain-wall-like mode $f_{\text{FMR-D}}$ modes, as shown in Fig. 2(c). Combining the saturation magnetization $M_s = 600 \text{ emu/cm}^3$ obtained from the $M - H$ loop above and the fitting of the dispersion relation f_{FMR} versus H_{res} using the Kittel formula $f = \gamma \sqrt{H[H + (4\pi M_s - H_k)]}$, we also obtain the interfacial perpendicular anisotropy field $H_k = 8.3 \text{ kOe}$.

C. Spectral characteristics of microwave generation

Magnetization auto-oscillation is observed when a sufficiently large dc current I_{dc} is applied to nanogap SHNO. Figure 2(d) shows representative auto-oscillation spectra acquired at $I = 10 \text{ mA}$ and room temperature $T = 295 \text{ K}$ with the field range from 0.3 to 2 kOe. The microwave power spectral density (PSD) and the central oscillation frequency can be determined by fitting the power spectra with the Lorentzian function. The oscillation frequency f_{auto} versus H dispersion relation suggests that the observed primary spin-wave mode is a propagating mode m_P with spin-wave emission because of its frequency f_{auto} above f_{FMR} obtained from the STFMR measurements [Fig. 2(c)]. We further investigate the detailed dependence of the spectral characteristics on the excitation current I at different external magnetic fields H and room temperature, as shown in Fig. 3. For all current-dependent spectra obtained at different magnetic fields H , the auto-oscillation frequency is above f_{FMR} and a significant frequency blueshift is observed with increasing current. In this Pt/[Co/Ni]-based SHNO with a strong PMA, such a large positive current-modulated frequency rate (approximately 150–200 MHz/mA) indicates that SOT-driven magnetization dynamics have a strong nonlinear

coefficient, which can be used to optimize the synchronization map in SHNO networks for neuromorphic computing via individual oscillator electrical control [27,45].

For all these magnetic field- and current-dependent microwave-generation spectra obtained at room temperature, only one dynamical mode is observed, which seems to be different from the above STFMR spectra of SHNO with a primary f_{FMR} and minor $f_{\text{FMR-D}}$ modes. To explore the underlined reason for the difference between self-generated microwave and STFMR spectra, we repeat the generated microwave spectroscopic measurements at a cryogenic temperature $T = 150 \text{ K}$, where thermal effects are significantly reduced, and the energy barrier for the nucleation or annihilation of the bubble and stripe domain is considerably enhanced.

Figure 4 shows the dependence of the spectral characteristics on I at the four selected fields $H = 0.5, 1.0, 1.5,$ and 2.0 kOe , which exhibits a similar overall evolution with the excitation current I . The representative spectra obtained at $H = 1.5 \text{ kOe}$ are taken as an example to illustrate current-dependent generation characteristics at $T = 150 \text{ K}$ [Fig. 4(e)–(g)]. At the onset current $I_{\text{on}} = 12 \text{ mA}$, the frequency $f = 2.8 \text{ GHz}$ of the primary mode m_P is near the primary FMR $f_{\text{FMR}} = 2.8 \text{ GHz}$. Above I_{on} , the primary oscillation peak exhibits a significant blueshift, a rapid increase of power, and a linear decrease of the linewidth with increasing I to the maximum peak power P_{peak} at the current $I_P = 16.5 \text{ mA}$. After passing I_P , P_{peak} starts to decrease significantly with I , while the frequency f still keeps a gradual blueshift and the linewidth FWHM continually decreases to a minimum value of 10 MHz at the same current $I = 17.75 \text{ mA}$ as the maximum frequency of 3.87 GHz and a relatively small power P_{peak} . The currents

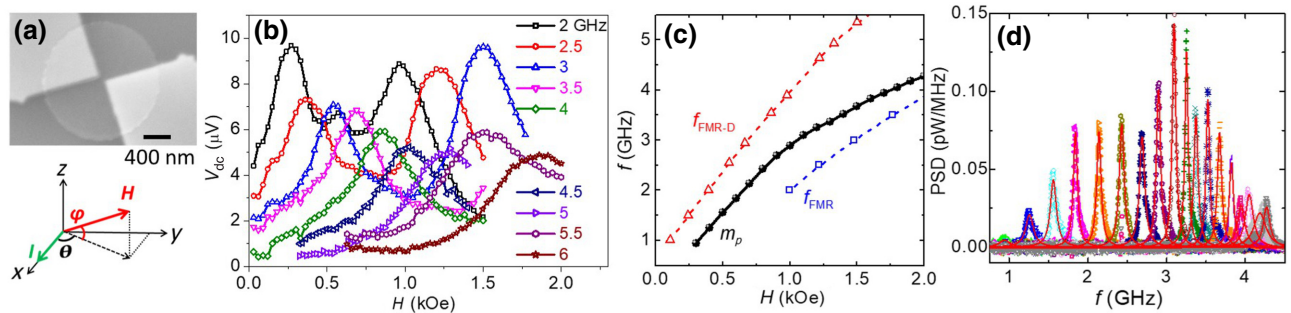


FIG. 2. Dynamical properties of nanogap SHNO with a strong PMA Pt/[Co/Ni] external film at 295 K, $\theta = 60^\circ$, and $\varphi = 5^\circ$. (a) Top: the SEM image of nanogap SHNO composed of a 2- μm -diameter Pt(4)/[Ni(0.3)/Co(0.2)]₄ multilayer disk and 100-nm-thick two triangular Au electrodes separated by an approximately 100-nm gap. Bottom: definition of the orientational angles θ and φ of the external magnetic field H . (b) STFMR voltage V_{dc} versus in-plane field H obtained with various excitation frequencies labeled in the panel. (c) The frequencies of the auto-oscillation mode m_P (black sphere) and the two FMR modes, corresponding to the FMR mode of the primary PMA regime f_{FMR} (blue square) and the in-plane magnetization domain region $f_{\text{FMR-D}}$ (red triangle), as a function of the field H . f_{FMR} and $f_{\text{FMR-D}}$ are determined by fitting the STFMR spectra in (b) with the Lorentzian function. The frequency of m_P is extracted from the microwave-generation spectra in (d). (d) Microwave-generation spectra (symbols) obtained at H between 0.3 and 2.0 kOe increased in 100 Oe steps, and the applied current $I = 10 \text{ mA}$. The curves are the results of fitting with the Lorentzian function.

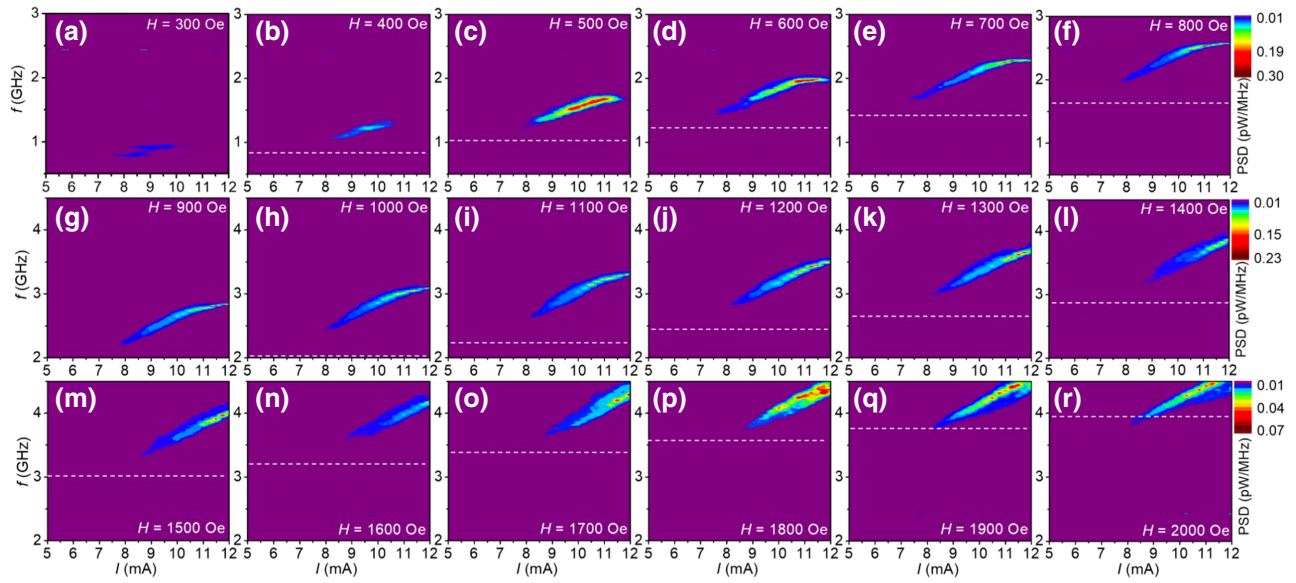


FIG. 3. (a)–(r) Pseudocolor maps of the dependence of the generated microwave spectra on the current at $T = 295$ K, H from 0.3 to 2.0 kOe increased in 100 Oe steps, labeled in the panels. Dashed horizontal lines represent the frequency f_{FMR} of the bulk FMR mode, determined by the STFM technique above.

larger than 18 mA begin to break the system balance and degrade oscillation coherence, accompanied by an obvious frequency redshift, a dramatic linewidth broadening, and a significant power dropping.

The nonlinear theory for single-mode auto-oscillator proves that the linewidth is inversely proportional to the oscillation power, which is determined by a combination of the auto-oscillation area and the amplitude of the

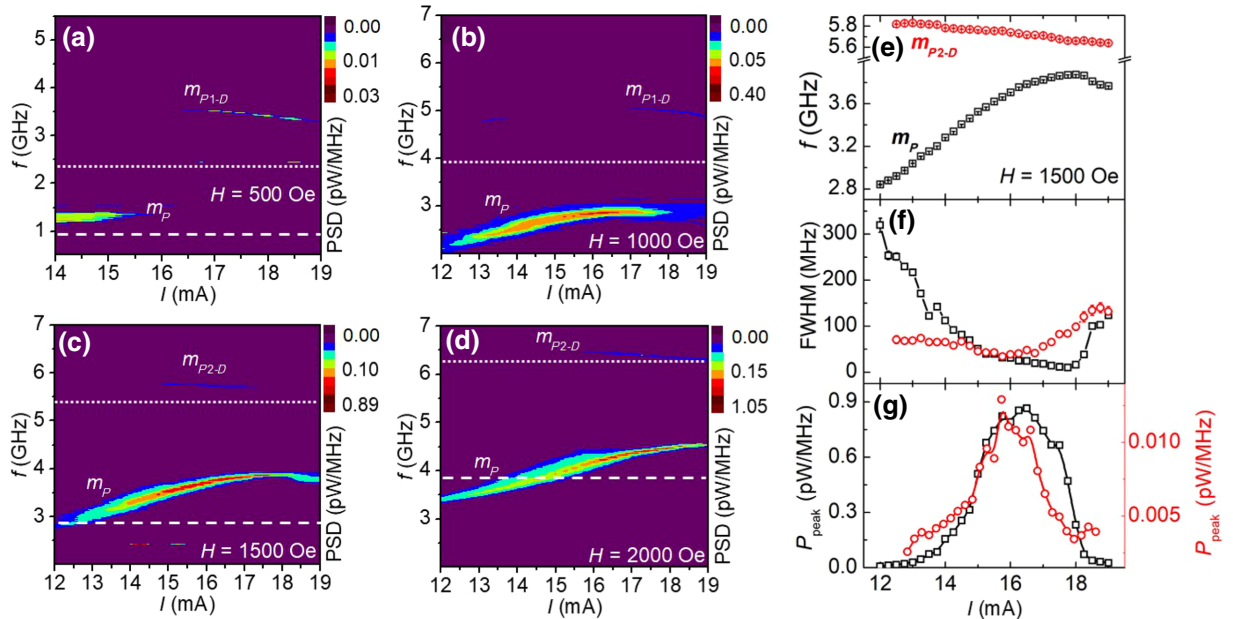


FIG. 4. (a)–(d) Pseudocolor maps of the dependence of the generated microwave spectra on the current at $T = 150$ K, at $H = 500$ (a), 1000 (b), 1500 (c), and 2000 Oe (d). (e)–(g) The current dependence of the central generation frequency f (e), the FWHM (f), and the intensity peak P_{peak} (g) of the dominant modes labeled m_P and m_{P2-D} . The spectral characteristics in (e)–(g) are extracted from the multipeak Lorentzian fitting of the spectra obtained at $H = 1500$ Oe. The corresponding frequencies of the primary FMR f_{FMR} and domain or domain wall-like resonance $f_{\text{FMR-D}}$ are marked by the dashed horizontal and dotted lines, respectively. m_P , m_{P1-D} , and m_{P2-D} mark the three distinct modes, as defined in the text, in the generated microwave spectra.

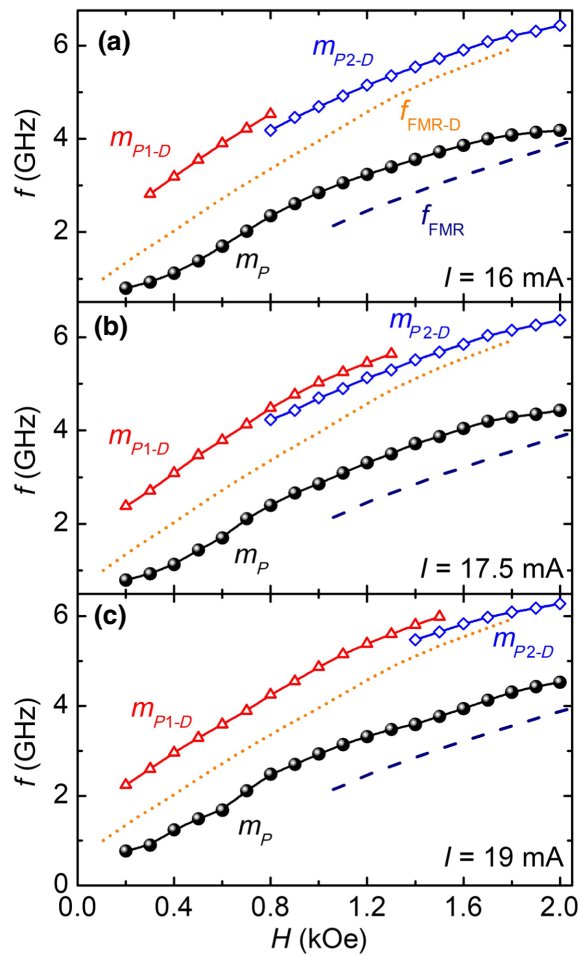


FIG. 5. The frequencies of the auto-oscillation modes of SHNO and its STFMR modes as a function of the magnetic field H , obtained at $T = 150$ K and three selected currents $I = 16$ mA (a), 17.5 mA (b), and 19 mA (c). f_{FMR} (dash line) and $f_{\text{FMR-D}}$ (dash-dot line) represent the FMR modes of the primary PMA regime and tiny domain or domain-wall regions, while m_P (black sphere), m_{P1-D} (red triangle), and m_{P2-D} (blue diamond) mark the three distinct modes, as the same as Fig. 4.

auto-oscillation. Meanwhile, the nonlinearity coefficient of the auto-oscillation also has a strong influence on the linewidth via the coupling between the amplitude and the phase noise. Therefore, the significant decrease of the linewidth at $I_{\text{on}} \leq I \leq I_P$ is related to the rapid increase of the generation power, consistent with this nonlinear theory. The further reduction of the linewidth at $I_P \leq I \leq 18$ mA is attributed to the phase-noise decrease due to the nonlinear frequency blueshift beginning weak.

Besides the primary oscillation peaks with a frequency above f_{FMR} of the primary PMA regime, another oscillation peak with a much weaker power intensity and a higher frequency than $f_{\text{FMR-D}}$, is also observed at large currents. In contrast to the primary peak with a significant blueshift, this high-frequency oscillation peak exhibits a relatively weak redshift with increasing current, and its

power intensity P_{peak} is approximately 100 times smaller than that of the primary mode [Figs. 4(e)–4(g)]. By combining the STFMR results and these spectra characteristics, we infer that this secondary peak is related to current-induced dynamics of the nanoscale IM domain region or thin domain wall appeared in the grain boundary, labeled as m_{P1-D} or m_{P2-D} , which is also supported by the discrete frequency jump behavior in the following dispersion relation between the oscillation frequency f and H .

Since the static magnetization structure of the Pt/[Co/Ni] multilayer with a strong PMA depends on the in-plane field [see the discussion of Fig. 1(b)], one can expect that the minor domain mode exhibits different magnetic field-dependent dynamical behaviors. Therefore, we carefully investigate the detailed dependence of the oscillation frequency on the magnetic field with three representative driving currents $I = 16, 17.5,$ and 19 mA, at $T = 150$ K in Fig. 5. Similar to the observations at $T = 295$ K [Fig. 2(d)], the primary oscillation peak m_P with the frequency above f_{FMR} of the primary FMR mode exhibits a consecutive dispersion relation with the field, rather than the abrupt jump of the oscillation frequency due to the transition from the quasilinear propagating spin-wave mode m_P to the self-localized bullet mode in our previous Pt/[Co/Ni]₆-based SHNO with a moderate PMA at $T = 140$ K [35]. However, after carefully analyzing the field dependence of the secondary high-frequency peak, we find that the frequencies of the oscillation peaks obey the two different dispersion curves for the low- and high-field ranges. For instance, the minor domain mode has a frequency jump from the high-frequency mode m_{P1-D} to the low-frequency mode m_{P2-D} at $H \sim 0.8$ kOe for $I = 16$ mA [Fig. 5(a)], two-mode coexistence at $0.8 \text{ kOe} \leq H \leq 1.3$ kOe for $I = 17.5$ mA [Fig. 5(b)], and at $1.4 \text{ kOe} \leq H \leq 1.5$ kOe for $I = 19$ mA [Fig. 5(c)]. It is attributed to the suppression of frequency of the domain mode by the applied external field, consistent with the current-dependent generated spectra with different fields in Fig. 4, where m_{P1-D} has a frequency far higher than f_{FMR} and more significant redshift than m_{P2-D} . Compared to the primary low-frequency propagating mode m_P , these secondary oscillation peaks have much weaker power intensity, indicating that they have a small oscillation area, while their higher frequencies than m_P may be correlated with the in-plane magnetization of the confined domain or domain wall [46] and the strong local demagnetization fields. All these current- and field-dependent generated microwave characteristics of the weak high-frequency peaks are consistent with the feature of spin current-driven auto-oscillation of a nanoscale in-plane magnetization domain or domain wall.

To gain further insight into the thermal effects on these current-driven magnetic dynamics, we repeat the current-dependent spectroscopic measurements at $H = 1.1$ kOe and different cryogenic temperatures, as shown in Fig. 6. The high-frequency domain-wall-like mode begins to be

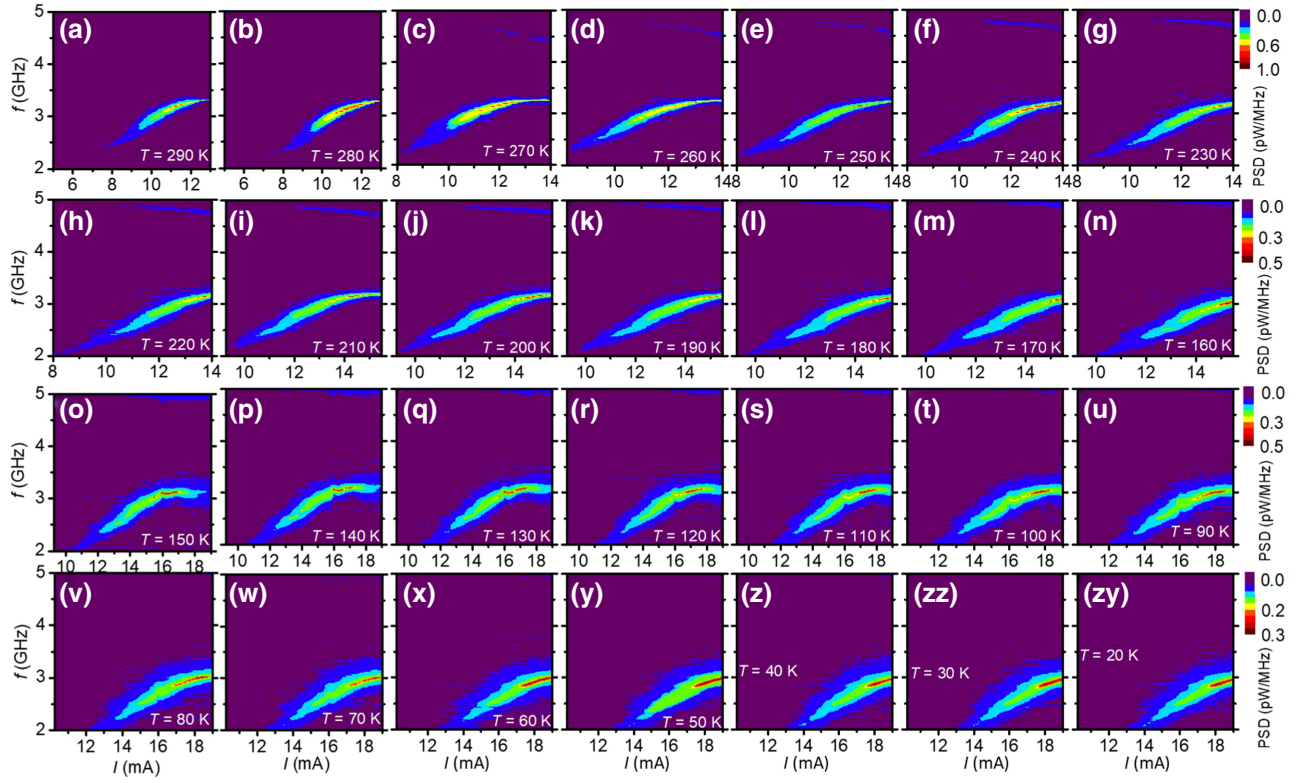


FIG. 6. (a)–(zy) Pseudocolor maps of the dependence of the generated microwave spectra on the excitation current I at $H = 1100$ Oe, and temperature T between 290 and 20 K with a step of 10 K, labeled in the panels.

observed at 270 K, and its oscillation frequency increases with decreasing temperature [Fig. 7(c)], and even its minimum frequency goes beyond the settled spectroscopic measurement maximum frequency of 5 GHz at 110 K [Fig. 6(s)]. The significant temperature-dependent oscillation frequency is associated with the substantial enhancement of the effective perpendicular anisotropy field H_k and the coercive field with decreasing temperature, which provides further evidence of the weak high-frequency peak associating with spin current-induced domain-wall-like mode. In contrast, the primary propagating mode m_p and the primary FMR mode show a slight decrease in their characteristic frequencies with reducing the temperature [Fig. 7(c)], indicating that a decrease of the [Co/Ni] magnetization \mathbf{M} does not significantly affect the dynamics of m_p .

Similar to the prior Pt-based SHNOs, the significant decrease of the onset current from 13 mA at $T = 20$ K to less than 7.5 mA at room temperature [Fig. 7(a)] indicates the apparent increase of the excitation efficiency at higher temperatures [2], which is likely correlated with the substantial decrease of the spin memory loss coefficient δ at Pt/Co interface with increasing temperature, which has been revealed by first-principles scattering theory [47]. Moreover, in contrast to the exponential or linear increase of linewidth on temperature [2,29,48–53], the linewidth

of the primary mode m_p exhibits a noticeable broadening with decreasing temperature [Fig. 7(b)], indicating that the linewidth is dominated by the frequency drift instability in this case. It is associated with the spatial inhomogeneity of the magnetic energy landscape, e.g., the local variations of PMA and the asymmetry of the effective magnetic field due to the dipole fields or stray fields generated by the bubble domains outside the active device nanogap region. Unlike the in-plane magnetized nanogap SHNOs [2,48], the studied PMA nanogap SHNO can significantly suppress the strong thermal broadening of linewidth at room temperature dominated by thermally activated mode transitions and/or thermal noise. It enables us to achieve a well-coherent propagating spin-wave emission with a small linewidth of 4 MHz at room temperature.

III. MICROMAGNETIC SIMULATIONS OF AUTO-OSCILLATION

To further confirm and obtain more insight into the experimentally observed propagating spin-wave mode, we perform micromagnetic simulations using oommf [54] for a circular Co/Ni disk with a diameter of 1 μm divided into $5 \times 5 \times 2 \text{ nm}^3$ cells. Similar to our prior work about Py/Pt-based SHNO [28], the simulation includes the effects of spin torque and the Oersted field produced by current,

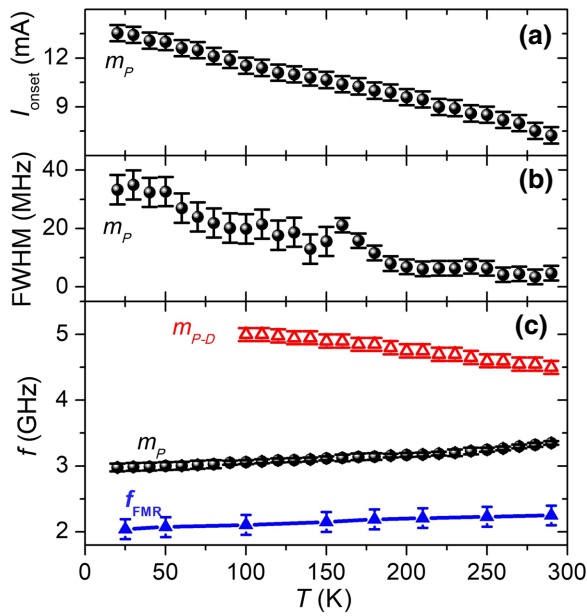


FIG. 7. Dependence of the generated microwave spectra with $H = 1100$ Oe in Fig. 6 on the temperature T . (a) Temperature dependence of the onset current of the primary propagating mode m_p . (b) Dependence of the minimum linewidth of m_p on T . (c) The minimum frequency of m_D , the maximum frequency of m_{p-D} and the FMR frequency f_{FMR} as a function of T .

both calculated with the COMSOL Multiphysics simulations [28]. Firstly, the effects of finite temperature and magnetic inhomogeneities or defects on forming and pinning domains are ignored for exploring the primary propagating mode. The material parameters used in the simulations are as follows: saturation magnetization $M_s = 600$ kA/m, anisotropy constant $K_u = 2.5 \times 10^5$ J/m³, Gilbert-damping constant $\alpha = 0.03$, spin Hall efficiency $P = 0.05$, and exchange stiffness $A = 10$ pJ/m. Figure 8(a) shows the representative calculated auto-oscillation spectra obtained by micromagnetic simulations with different excitation currents at the magnetic field $H = 2$ kOe tilted by angle $\varphi = 5^\circ$ relative to the film plane and forming in-plane angle $\theta = 60^\circ$ with the direction of the current flow, values similar to those used in some of the measurements discussed above. The current-dependent spectra are well consistent with our experimentally observed primary mode characterized by the auto-oscillation frequency above f_{FMR} and a significant frequency blueshift with the increasing current in Fig. 3(r).

To gain more insight into the spatial characteristics of this dynamical mode, we also calculate the normalized spatial power maps of the observed dynamical mode, obtained from the time dependence of the local magnetization component m_z^2 by our performing pointwise temporal fast Fourier transform (FFT) over the simulated area of the Co/Ni disk. Figure 8(b) shows that the dynamical

mode exhibits a symmetric elongated spatial profile along the magnetic field and circular intensity modulations consistent with spin-wave radiation from the active device region. Time sequences of \mathbf{M} allow us to visually see the spreading process of the spin waves from the active nanogap region. Figures 8(c)–8(g) show five representative snapshots of the distribution of instantaneous \mathbf{M} for excitation current $I = 7.2$ mA and $H = 2$ kOe, indicating the oscillation period τ is approximately 0.2 ns, corresponding to 5.07 GHz obtained by FFT in Fig. 8(a). These time sequences of pseudocolor map \mathbf{M} show a propagating spin wave characterized by a near isotropic propagation velocity and $\lambda \sim 0.25$ μm spin-wave wavelength. The generated propagating spin-wave mode has a larger amplitude at the direction parallel with the in-plane component of the magnetic field H_{in} , which is similar to the spatial profile of the second harmonic of the primary center mode in the in-plane magnetized nanogap SHNO [28]. The second-harmonic frequency is above f_{FMR} , within the linear spectrum of propagating spin waves. In these nanogap SHNOs, the previous studies have proved that the time-average internal magnetic field $\langle H_{\text{int}} \rangle_t$ has two local minima, offset from the device center in two opposition directions collinear with the external field [28,55]. These minima are caused by the dipolar field produced by the center mode, which creates a channel collinear with H to facilitate spin-wave propagating, or forms the secondary mode via nonlinear mode coupling in the in-plane magnetized nanogap SHNOs.

Next, to model the secondary dynamical mode likely correlating to the confined magnetic domain, we assume that there exists an elliptical region with a weaker PMA constant $K_u = 1.8 \times 10^5$ J/m³ near the central nanogap between two triangular Au electrodes after considering the grain-boundary effect of polycrystalline multilayer film and possible defects. In addition, to weaken the strong exchange coupling between this confined domain and its surrounding area due to grain-boundary degenerated effect, A is set to 1 pJ/m for 6 nm wider annular border [56]. The major and minor axis of the ellipse is set to approximately 80 and 30 nm, respectively. To obtain more refined simulation results, we discretize a Co/Ni disk with 2 nm thickness and 400 nm in diameter using a finer grid of cubic cells of 2 nm. Other simulation parameters are the same as above. Figure 9(a) shows the representative calculated auto-oscillation spectra as a function of excitation current I at $H = 2$ kOe, $\varphi = 5^\circ$, and $\theta = 60^\circ$. There are two distinct dynamical modes with different frequencies (approximately 4 and 7 GHz) and opposite current-induced frequency shift trends in the calculated spectra, well consistent with the experimentally observed primary propagating mode m_p with a low frequency and significant blueshift, and the secondary high-frequency mode m_{p-D} with a frequency redshift in Fig. 4(d). Moreover, Figs. 9(b) and 9(c) show the spatial characteristics of these two

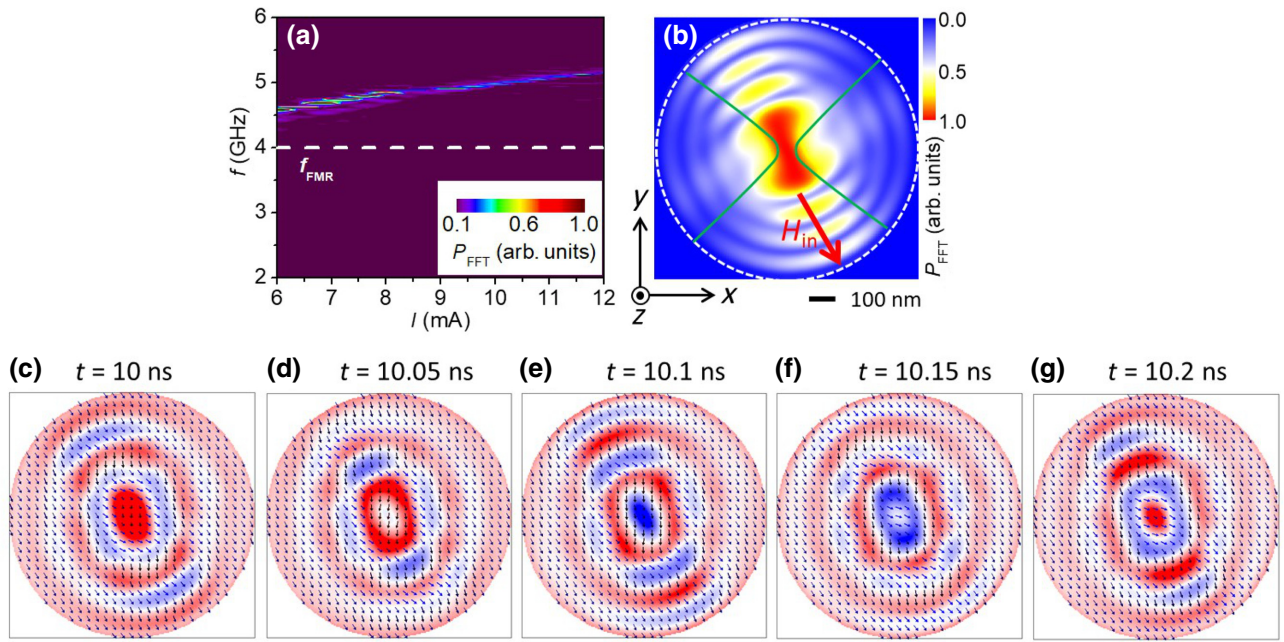


FIG. 8. Micromagnetic simulation of the nanogap SHNO without regarding the defect-induced magnetic domain. (a) Pseudocolor map of the calculated power spectral density as a function of excited current I at $H = 2$ kOe, $\theta = 60^\circ$, and $\varphi = 5^\circ$. The dashed horizontal line represents the FMR frequency f_{FMR} . (b) Normalized spatial maps of the square of the simulated dynamical magnetization component M_z^2 of the auto-oscillation mode $f = 5.07$ GHz at $I = 7.2$ mA. The large dashed circle represents the boundary of the active simulation region, the two green curves mark the positions of the two top triangle Au electrodes, and the arrow shows the direction of the near in-plane field H_{in} . (c)–(g) Time sequences of out-of-plane (in color) and in-plane (vector) magnetization components obtained from micromagnetic simulations at $I = 7.2$ mA and field $H = 2$ kOe. FFT, fast Fourier transform.

dynamical modes m_P and m_{P-D} , respectively, with the same method used in Fig. 8(b) above. The propagating mode m_P shows an extended spatial distribution of power density, but except for the elliptical in-plane magnetization domain region with a small PMA field less than the demagnetization field. In contrast, the high-frequency mode m_{P-D} is

excited in the elliptical region. Although the power density is most localized in the elliptical IM domain, it also exhibits obvious intensity modulation in its surrounding medium, indicating the spin-wave radiation of this mode. This spin-wave emission into the surrounding area is consistent with the fact that its frequency $f_{P-D} = 7.26$ GHz is

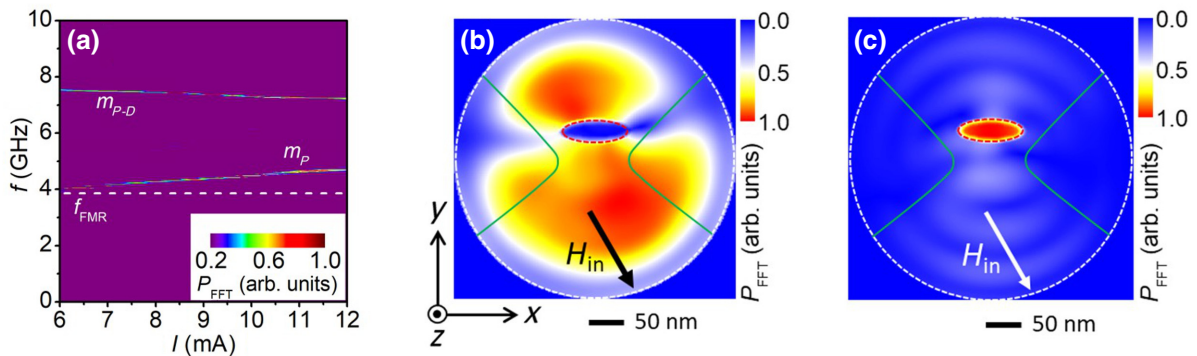


FIG. 9. Micromagnetic simulation of the nanogap SHNO with a nanoscale magnetic domain. (a) Pseudocolor map of dependence of the calculated power spectra on current I at $H = 2$ kOe, $\theta = 60^\circ$, and $\varphi = 5^\circ$. The dashed horizontal line represents the primary FMR frequency f_{FMR} . (b) and (c) Normalized spatial maps of M_z^2 of two auto-oscillation modes m_P with $f = 4.53$ GHz (b) and m_{P-D} with $f = 7.26$ GHz (c) at $I = 10.4$ mA. The large dashed circle represents the boundary of the active simulation region (400-nm diameter), the small dashed ellipse marks the position of the area with a small $K_u = 1.8 \times 10^5$ J/m³, the two green curves mark the positions of two top triangle Au electrodes, and the arrow shows the direction of the near in-plane field H_{in} .

higher than $f_{\text{FMR}} = 4$ GHz of its surrounding medium with a large PMA [37,38,57].

IV. CONCLUSION

To summarize, we observe two distinct dynamical modes in the planar nanogap SHNO based on Pt/[Co/Ni]₄ with a large PMA field of $H_k = 8.3$ kOe at in-plane field geometry using microwave spectroscopy. The primary lower-frequency peak is a bulk propagating spin-wave mode corresponding to the perpendicular magnetization region. It exhibits a frequency near f_{FMR} at the small currents, above f_{FMR} at the large currents, and a significant frequency blueshift with increasing current. The secondary high-frequency mode with a much weaker power intensity coexists with the primary propagating mode at the low fields of less than 2 kOe and a certain current. It exhibits a slight redshift with current and the discrete frequency jump or multi-peaks by varying magnetic fields. These spectra characteristics indicate that the latter is associated with the tiny domain or domain-wall region at the in-plane fields below the saturation field of Pt/[Co/Ni]₄ film. Furthermore, the temperature dependence of spectra shows that the propagating mode and the FMR mode both decrease their frequency by reducing temperature. In contrast, the high-frequency domain-wall-like mode increases its frequency with the temperature decrease. These temperature-dependent behaviors are related to the enhancement of the PMA field by reducing temperature. The minimum linewidth of the propagating mode gradually broadens from 5 MHz at 295 K to 36 MHz at 6 K, indicating that SOT-driven dynamical coherence in Pt/[Co/Ni]-based SHNO with a strong PMA is dominated by the frequency drift instability due to the pinning effect. It is in contrast to thermal noise that causes a linear or exponential linewidth broadening with increasing temperature due to thermal fluctuation, which are previously observed in the in-plane magnetized SHNOs. Moreover, our micromagnetic simulations reproduce the experimentally observed propagating and domain modes and provide the spatial profile of propagating spin-wave mode characterized by near isotropic propagation velocity or wavelength. Our results demonstrate the controllable propagating spin-waves in an external PMA magnetic film-based SHNO, which can facilitate building the SHNO network arrays with controllable nonlinear coupling for information processing via analog and neuromorphic computing.

ACKNOWLEDGMENTS

We acknowledge support from the National Natural Science Foundation of China (Grants No. 12074178, No. 12004171), the Applied Basic Research Programs of Science and Technology Commission Foundation of Jiangsu Province (Grant No. BK20200309), the Open Research

Fund of Jiangsu Provincial Key Laboratory for Nanotechnology, and the Scientific Foundation of Nanjing University of Posts and Telecommunications (NUPTSF) (Grant No. NY220164).

- [1] V. E. Demidov, S. Urazhdin, H. Ulrichs, V. Tiberkevich, A. Slavin, D. Baither, G. Schmitz, and S. O. Demokritov, Magnetic nano-oscillator driven by pure spin current, *Nat. Mater.* **11**, 1028 (2012).
- [2] R. H. Liu, W. L. Lim, and S. Urazhdin, Spectral Characteristics of the Microwave Emission by the Spin Hall Nano-Oscillator, *Phys. Rev. Lett.* **110**, 147601 (2013).
- [3] I. M. Miron, K. Garello, G. Gaudin, P. J. Zermatten, M. V. Costache, S. Auffret, S. Bandiera, B. Rodmacq, A. Schuhl, and P. Gambardella, Perpendicular switching of a single ferromagnetic layer induced by in-plane current injection, *Nature* **476**, 189 (2011).
- [4] T. Suzuki, S. Fukami, N. Ishiwata, M. Yamanouchi, S. Ikeda, N. Kasai, and H. Ohno, Current-induced effective field in perpendicularly magnetized Ta/CoFeB/MgO wire, *Appl. Phys. Lett.* **98**, 142505 (2011).
- [5] L. Liu, C.-F. Pai, Y. Li, H. W. Tseng, D. C. Ralph, and R. A. Buhrman, Spin-torque switching with the giant spin Hall effect of tantalum, *Science* **336**, 555 (2012).
- [6] G. Yu, P. Upadhyaya, Y. Fan, J. G. Alzate, W. Jiang, K. L. Wong, S. Takei, S. A. Bender, L.-T. Chang, Y. Jiang, M. Lang, J. Tang, Y. Wang, Y. Tserkovnyak, P. K. Amiri, and K. L. Wang, Switching of perpendicular magnetization by spin-orbit torques in the absence of external magnetic fields, *Nat. Nanotechnol.* **9**, 548 (2014).
- [7] J. C. Slonczewski, Current-driven excitation of magnetic multilayers, *J. Magn. Magn. Mater.* **159**, L1 (1996).
- [8] D. C. Ralph and M. D. Stiles, Spin transfer torques, *J. Magn. Magn. Mater.* **320**, 1190 (2008).
- [9] A. Hoffmann, Spin Hall effects in metals, *IEEE Trans. Magn.* **49**, 5172 (2013).
- [10] Jairo Sinova, Sergio O. Valenzuela, J. Wunderlich, C. H. Back, and T. Jungwirth, Spin Hall effects, *Rev. Mod. Phys.* **87**, 1213 (2015).
- [11] A. Manchon, J. Zelezny, I. M. Miron, T. Jungwirth, J. Sinova, A. Thiaville, K. Garello, and P. Gambardella, Current-induced spin-orbit torques in ferromagnetic and antiferromagnetic systems, *Rev. Mod. Phys.* **91**, 035004 (2019).
- [12] Z. H. Wang, Y. Y. Sun, M. Z. Wu, V. Tiberkevich, and A. Slavin, Control of Spin Waves in a Thin Film Ferromagnetic Insulator through Interfacial Spin Scattering, *Phys. Rev. Lett.* **107**, 146602 (2011).
- [13] M. Collet, X. de Milly, O. d'Allivy Kelly, V. V. Naletov, R. Bernard, P. Bortolotti, J. Ben Youssef, V. E. Demidov, S. O. Demokritov, J. L. Prieto, M. Munoz, V. Cros, A. Anane, G. de Loubens, and O. Klein, Generation of coherent spin-wave modes in yttrium iron garnet microdiscs by spin-orbit torque, *Nat. Commun.* **7**, 10377 (2016).
- [14] M. B. Jungfleisch, W. Zhang, J. Sklenar, J. Ding, W. Jiang, H. Chang, F. Y. Fradin, J. E. Pearson, J. B. Ketterson, V. Novosad, M. Wu, and A. Hoffmann, Large Spin-Wave Bullet in a Ferrimagnetic Insulator Driven by the Spin Hall Effect, *Phys. Rev. Lett.* **116**, 057601 (2016).

- [15] R. H. Liu, W. L. Lim, and S. Urazhdin, Dynamical Skyrmion State in a Spin Current Nano-Oscillator with Perpendicular Magnetic Anisotropy, *Phys. Rev. Lett.* **114**, 137201 (2015).
- [16] H. Mazraati, S. Chung, A. Houshang, M. Dvornik, L. Piazza, F. Qejvanaj, S. Jiang, T. Q. Le, J. Weissenrieder, and J. Åkerman, Low operational current spin Hall nano-oscillators based on NiFe/W bilayers, *Appl. Phys. Lett.* **109**, 242402 (2016).
- [17] T. Chen, R. K. Dumas, A. Eklund, P. K. Muduli, A. Houshang, A. A. Awad, P. Dürrenfeld, B. G. Malm, A. Rusu, and J. Åkerman, Spin-torque and spin-Hall nano-oscillators, *Proc. IEEE* **104**, 1919 (2016).
- [18] V. E. Demidov, S. Urazhdin, G. de Loubens, O. Klein, V. Cros, A. Anane, and S. O. Demokritov, Magnetization oscillations and waves driven by pure spin currents, *Phys. Rep.* **673**, 1 (2017).
- [19] L. Li, L. Chen, R. H. Liu, and Y. Du, Recent progress on excitation and manipulation of spin-waves in spin Hall nano-oscillators, *Chin. Phys. B* **29**, 117102 (2020).
- [20] N. Sato, K. Schultheiss, L. Körber, N. Puwenberg, T. Mühl, A. A. Awad, S. S. P. K. Arekapudi, O. Hellwig, J. Fassbender, and H. Schultheiss, Domain Wall Based Spin-Hall Nano-Oscillators, *Phys. Rev. Lett.* **123**, 057204 (2019).
- [21] T. Hache, Y. Li, T. Weinhold, B. Scheumann, F. J. T. Goncalves, O. Hellwig, J. Fassbender, and H. Schultheiss, Bipolar spin Hall nano-oscillators, *Appl. Phys. Lett.* **116**, 192405 (2020).
- [22] V. E. Demidov, H. Ulrichs, S. O. Demokritov, S. V. Gurevich, V. Tiberkevich, A. Slavin, A. Zholud, and S. Urazhdin, Synchronization of spin Hall nano-oscillators to external microwave signals, *Nat. Commun.* **5**, 3179 (2014).
- [23] T. Hache, T. Weinhold, K. Schultheiss, J. Stigloher, F. Vilsmeier, C. Back, S. S. P. K. Arekapudi, O. Hellwig, J. Fassbender, and H. Schultheiss, Combined frequency and time domain measurements on injection-locked, constriction-based spin Hall nano-oscillators, *Appl. Phys. Lett.* **114**, 102403 (2019).
- [24] F. J. T. Gonçalves, T. Hache, M. Bejarano, T. Hula, O. Hellwig, J. Fassbender, and H. Schultheiss, Agility of Spin Hall Nano-Oscillators, *Phys. Rev. Appl.* **16**, 054050 (2021).
- [25] A. A. Awad, P. Dürrenfeld, A. Houshang, M. Dvornik, E. Iacocca, R. K. Dumas, and J. Åkerman, Long-range mutual synchronization of spin Hall nano-oscillators, *Nat. Phys.* **13**, 292 (2017).
- [26] M. Zahedinejad, A. A. Awad, S. Muralidhar, R. Khymyn, H. Fulara, H. Mazraati, M. Dvornik, and J. Åkerman, Two-dimensional mutually synchronized spin Hall nano-oscillator arrays for neuromorphic computing, *Nat. Nanotechnol.* **15**, 47 (2020).
- [27] M. Zahedinejad, H. Fulara, R. Khymyn, A. Houshang, M. Dvornik, S. Fukami, S. Kanai, H. Ohno, and J. Åkerman, Memristive control of mutual spin Hall nano-oscillator synchronization for neuromorphic computing, *Nat. Mater.* **21**, 81 (2022).
- [28] L. Chen, K. Zhou, S. Urazhdin, W. Jiang, Y. W. Du, and R. H. Liu, Dynamical mode coexistence and chaos in the nanogap spin Hall nano-oscillator, *Phys. Rev. B* **100**, 104436 (2019).
- [29] L. Chen, S. Urazhdin, K. Zhou, Y. W. Du, and R. H. Liu, Magnetic Droplet Mode in a Vertical Nanocontact-Based Spin Hall Nano-Oscillator at Oblique Fields, *Phys. Rev. Appl.* **13**, 024034 (2020).
- [30] V. E. Demidov, S. Urazhdin, A. Zholud, A. V. Sadovnikov, and S. O. Demokritov, Nanoconstriction-based spin-Hall nano-oscillator, *Appl. Phys. Lett.* **105**, 172410 (2014).
- [31] H. Mazraati, S. R. Etesami, Seyed Amir Hossein Banuazizi, S. Chung, A. Houshang, A. A. Awad, M. Dvornik, and J. Åkerman, Auto-oscillating Spin-Wave Modes of Constriction-Based Spin Hall Nano-oscillators in Weak In-Plane Fields, *Phys. Rev. Appl.* **10**, 054017 (2018).
- [32] Z. Duan, A. Smith, L. Yang, B. Youngblood, J. Lindner, V. E. Demidov, S. O. Demokritov, and I. N. Krivorotov, Nanowire spin torque oscillator driven by spin orbit torques, *Nat. Commun.* **5**, 1038 (2014).
- [33] A. Slavin and V. Tiberkevich, Spin Wave Mode Excited by Spin-Polarized Current in a Magnetic Nanocontact is a Standing Self-Localized Wave Bullet, *Phys. Rev. Lett.* **95**, 237201 (2005).
- [34] B. Divinskiy, S. Urazhdin, V. E. Demidov, A. Kozhanov, A. P. Nosov, A. B. Rinkevich, and S. O. Demokritov, Magnetic droplet solitons generated by pure spin currents, *Phys. Rev. B* **96**, 224419 (2017).
- [35] L. Chen, S. Urazhdin, Y. W. Du, and R. H. Liu, Dynamical Mode Coupling and Coherence in a Spin Hall Nano-Oscillator with Perpendicular Magnetic Anisotropy, *Phys. Rev. Appl.* **11**, 064038 (2019).
- [36] A. Slavin and V. Tiberkevich, Nonlinear auto-oscillator theory of microwave generation by spin-polarized current, *IEEE Trans. Magn.* **45**, 1875 (2009).
- [37] M. Evelt, L. Soumah, A. Rinkevich, S. Demokritov, A. Anane, V. Cros, J. Ben Youssef, G. de Loubens, O. Klein, P. Bortolotti, and V. Demidov, Emission of Coherent Propagating Magnons by Insulator-Based Spin-Orbit-Torque Oscillators, *Phys. Rev. Appl.* **10**, 041002(R) (2018).
- [38] H. Fulara, M. Zahedinejad, R. Khymyn, A. A. Awad, S. Muralidhar, M. Dvornik, and J. Åkerman, Spin-orbit torque-driven propagating spin waves, *Sci. Adv.* **5**, eaax8467 (2019).
- [39] H. Fulara, M. Zahedinejad, R. Khymyn, M. Dvornik, S. Fukami, S. Kanai, H. Ohno, and J. Åkerman, Giant voltage-controlled modulation of spin Hall nano-oscillator damping, *Nat. Commun.* **11**, 4006 (2020).
- [40] A. Kumar, M. Rajabali, V. H. Gonzalez, M. Zahedinejad, A. Houshang, and J. Åkerman, Fabrication of voltage-gated spin Hall nano-oscillators, *Nanoscale* **14**, 1432 (2022).
- [41] J.-G. Choi, J. Park, M.-G. Kang, D. Kim, J.-S. Rieh, K.-J. Lee, K.-J. Kim, and B.-G. Park, Voltage-driven gigahertz frequency tuning of spin Hall nano-oscillators, *Nat. Commun.* **13**, 3783 (2022).
- [42] C. Yan, L. Chen, K. Zhou, L. Yang, Q. Fu, W. Wang, L. Liang, Z. Tao, J. Du, Y. Wang, and R. H. Liu, Thickness-dependent magnetic properties in Pt/[Co/Ni]_n multilayers with perpendicular magnetic anisotropy, *Chin. Phys. B* **32**, 017503 (2023).
- [43] V. P. Amin, P. M. Haney, and M. D. Stiles, Interfacial spin-orbit torques, *J. Appl. Phys.* **128**, 151101 (2020).

- [44] W. Wang, G. Zhu, K. Zhou, X. Zhan, Z. Tao, Q. Fu, L. Liang, Z. Li, L. Chen, C. Yan, H. Li, T. Zhou, and R. H. Liu, Enhancement of spin-orbit torque efficiency by tailoring interfacial spin-orbit coupling in Pt-based magnetic multilayers, *Chin. Phys. B* **31**, 097504 (2022).
- [45] R. H. Liu, Lina Chen, S. Urazhdin, and Y. W. Du, Controlling the Spectral Characteristics of a Spin-Current Auto-Oscillator with an Electric Field, *Phys. Rev. Appl.* **8**, 021001(R) (2017).
- [46] G. Chen, T. Ma, A. T. N'Diaye, H. Kwon, C. Won, Y. Wu, and A. K. Schmid, Tailoring the chirality of magnetic domain walls by interface engineering, *Nat. Commun.* **4**, 2671 (2013).
- [47] K. Gupta, R. J. H. Wesselink, R. X. Liu, Z. Yuan, and P. J. Kelly, Disorder Dependence of Interface Spin Memory Loss, *Phys. Rev. Lett.* **124**, 087702 (2020).
- [48] L. Chen, Y. Gu, K. Zhou, Z. Li, L. Li, Z. Gao, Y. W. Du, and R. H. Liu, Temperature and electric field effects on the dynamic modes in a spin current auto-oscillator, *Phys. Rev. B* **103**, 144426 (2021).
- [49] V. S. Tiberkevich, A. N. Slavin, and J. V. Kim, Temperature dependence of nonlinear auto-oscillator linewidths: Application to spin-torque nano-oscillators, *Phys. Rev. B* **78**, 092401 (2008).
- [50] T. J. Silva and M. W. Keller, Theory of thermally induced phase noise in spin torque oscillators for a high-symmetry case, *IEEE Trans. Magn.* **46**, 3555 (2010).
- [51] M. L. Schneider, W. H. Rippard, M. R. Pufall, T. Cecil, T. J. Silva, and S. E. Russek, Temperature dependence of spin-torque-driven self-oscillations, *Phys. Rev. B* **80**, 144412 (2009).
- [52] J. F. Sierra, M. Quinsat, F. Garcia-Sanchez, U. Ebels, I. Joumard, A. S. Jenkins, B. Dieny, M. C. Cyrille, A. Zeltser, and J. A. Katine, Influence of thermal fluctuations on the emission linewidth in MgO-based spin transfer oscillators, *Appl. Phys. Lett.* **101**, 062407 (2012).
- [53] P. Bortolotti, A. Dussaux, J. Grollier, V. Cros, A. Fukushima, H. Kubota, K. Yakushiji, S. Yuasa, K. Ando, and A. Fert, Temperature dependence of microwave voltage emission associated to spin-transfer induced vortex oscillation in magnetic tunnel junction, *Appl. Phys. Lett.* **100**, 042408 (2012).
- [54] M. J. Donahue and D. G. Porter, OOMMF (NIST), <http://math.nist.gov/oommf>.
- [55] H. Ulrichs, V. E. Demidov, and S. O. Demokritov, Micro-magnetic study of auto-oscillation modes in spin-Hall nano-oscillators, *Appl. Phys. Lett.* **104**, 042407 (2014).
- [56] C. C. M. Capriata, S. Jiang, J. Åkerman, and B. G. Malm, Impact of random grain structure on spin-Hall nano-oscillator modal stability, *IEEE Electron Device Lett.* **43**, 312 (2022).
- [57] V. E. Demidov, S. Urazhdin, R. H. Liu, B. Divinskiy, A. Teletin, and S. O. Demokritov, Excitation of coherent propagating spin waves by pure spin currents, *Nat. Commun.* **7**, 10446 (2016).